

## Article

# The High-Pressure Methane/Brine/Quartz Contact Angle and Its Influence on Gas Reservoir Capillaries

Hua Tian <sup>1,2,3,\*</sup> , Junjia Fan <sup>1,4</sup> , Zhichao Yu <sup>1,2,3,\*</sup> , Qiang Liu <sup>5</sup>  and Xuesong Lu <sup>1,4</sup> <sup>1</sup> Research Institute of Petroleum Exploration and Development, PetroChina, Beijing 100083, China<sup>2</sup> National Energy Tight Oil and Gas R & D Center, Beijing 100083, China<sup>3</sup> CNPC Key Laboratory of Oil and Gas Reservoir, Beijing 100083, China<sup>4</sup> CNPC Key Laboratory of Basin Structure and Hydrocarbon Accumulation, Beijing 100083, China<sup>5</sup> Exploration and Development Research Institute, Daqing Oilfield Co., Ltd., Daqing 163712, China

\* Correspondence: tianhua86@petrochina.com.cn (H.T.); yuzhichao@petrochina.com.cn (Z.Y.);

Tel.: +86-10-83593518 (H.T.); +86-10-83599256 (Z.Y.)

**Abstract:** A capillary high-pressure optical cell (HPOC) combined with a confocal Raman system was used in this study of high-pressure methane/brine contact angles on a quartz surface. The contact angle was determined from the shape of the methane/brine/quartz interface; it increased with fluid pressure from 41° to 49° over a pressure range of 5.7–69.4 MPa. A linear relationship between the contact angle and the Raman shift was also observed. The experimentally measured contact angle was more accurately applied in calculations of capillary resistance than the empirically estimated 0°, and it provides an important parameter in the study of gas migration and production processes. For a natural gas reservoir, pore-throat capillary resistance was 33% lower than the traditionally accepted value, and low capillary resistance is conducive to deeply buried tight gas reservoirs becoming more gas saturated. As burial depth increases, capillary resistance initially decreases and passes through a maximum before decreasing again, rather than increasing linearly with depth. Our results provide critical parameters for gas reservoir production, modeling, and resource assessment. This non-destructive method may be useful for predicting contact angles through measurement of the Raman shift of the HPOC and fluid inclusions in the reservoir.

**Keywords:** contact angle; wettability; methane; high pressure; tight reservoir; Raman spectra

**Citation:** Tian, H.; Fan, J.; Yu, Z.; Liu, Q.; Lu, X. The High-Pressure Methane/Brine/Quartz Contact Angle and Its Influence on Gas Reservoir Capillaries. *Minerals* **2023**, *13*, 164. <https://doi.org/10.3390/min13020164>

Academic Editor: Tuncel M. Yegulalp

Received: 16 November 2022

Revised: 13 January 2023

Accepted: 16 January 2023

Published: 23 January 2023



**Copyright:** © 2023 by the authors. Licensee MDPI, Basel, Switzerland. This article is an open access article distributed under the terms and conditions of the Creative Commons Attribution (CC BY) license (<https://creativecommons.org/licenses/by/4.0/>).

## 1. Introduction

Pressure-driven volume flow is an efficient mechanism of natural gas migration. Pores in a formation may originally be saturated with brine, in which gas gradually displaces during the charging process [1–3]. In the multiphase fluid regimes of petroleum systems, gas enters the reservoir when the capillary entry pressures of natural gas flow are exceeded, at a rate depending on intrinsic and relative permeability [4–6]. Brine in larger pores is displaced by gas before the brine in smaller pores with higher capillary pressures [7,8]. Wettability, indicated by the gas/brine contact angle, has a strong influence on reservoir capillary pressures and is a critical parameter influencing immiscible fluid behavior in gas reservoirs [9,10]. Wettability influences capillary pressure, relative permeability, and multiphase fluid distribution at the pore scale [11,12]. For a gas/brine system with cylindrical capillaries, the contact angle,  $\theta$ , is related to capillary pressure,  $P_c$ , by the Young–Laplace equation [13]:

$$P_c = \frac{2\gamma_{lg} \cos \theta_{lg}}{r} \quad (1)$$

where  $\gamma_{lg}$  is the interfacial tension (IFT) between brine and gas, and  $r$  is the average pore radius. Strong wetting occurs as  $\theta$  approaches zero ( $\cos \theta = 1$ ), yielding the highest capillary pressures [14,15]. As  $\theta$  approaches 90° ( $\cos \theta = 0$ ), the two interfaces involving the solid

surface have equal interfacial tensions [16,17]. Less-wet reservoirs may have lower critical capillary pressures, higher gas saturation, and larger gas resources [17–20].

An understanding of basic reservoir properties such as porosity, permeability, pore size distribution, and (most importantly) wettability is critical for fluid transport [21]. The key role of wettability in the mobility of different fluid phases is an important research topic in petroleum engineering. Wettability is key to understanding the capacity of a reservoir to store hydrocarbon gas over geological timescales [22]. Deeply buried gas reservoirs are tight under high-pressure conditions (>45 MPa) associated with a thick overburden [23]. The high capillary resistance of small pore throats may reduce gas saturation. Capillary resistance is in turn determined by wettability and interfacial tension, with the gas/brine contact angle being a key factor in gas resource assessment. In the case of deeply buried sandstone gas reservoirs, quartz grains and quartz cement are the most important porous minerals, along with small amounts of carbonate, feldspar, and clay minerals [24]. Smooth silicate mineral (represented by quartz) surfaces are always adopted in contact-angle measurements; as the most common composition [25]. Methane is the most abundant hydrocarbon in gas reservoirs.

Most air/brine contact angles are measured under ambient conditions [26,27], and for smooth surfaces may range from 0° to 120° [28–30]. The contact angles of gases of different composition vary greatly even under the same test conditions. For example, extrapolation of behaviors from CH<sub>4</sub> to CO<sub>2</sub> must be avoided unless they have similar densities [31]. Previous studies have investigated wettability through the determination of brine/gas contact angles under different conditions on many types of mineral, including minerals under the effects of pressure, temperature, and brine salinity [32,33]. Pan et al. [34] observed that the contact angle at 323 K was slightly higher than that at 300 K. Air/brine contact angles increase with temperatures over the range from 35 °C to 70 °C [35]. The effect of temperature was attributed mainly to the decrease in the density difference between the two phases. Lower contact angles at higher temperatures have also been reported [36–38]. Temperature effects may thus cause increases or decreases in the contact angle, depending on other physical parameters such as pressure, surface charge, and pH [35]. Theoretically, contact-angle variations with temperature are linked to changes in the density of fluids and van der Waals forces [39].

High-pressure methane/brine contact angles have been reported for pressures of <20 MPa, increasing with pressure for CH<sub>4</sub>/brine/quartz systems. The CH<sub>4</sub>/brine contact angle increases from 0° to 30° and 34.8° at 300 K and 323 K, respectively, with pressures of 0.1–20 MPa [34]. An increase in pressure to 20 MPa from ambient conditions also increases the gas/brine contact angle [27]. The increase in the contact angle at high pressures has been attributed to a reduced density difference between the two fluid phases [40]. An empirical methane/brine contact angle of 0° ( $\cos\theta = 1$ ) has commonly been used with the premise that reservoir pore throats are strongly water-wet [41]. However, a comprehensive study with a wide range of pressures up to 65 MPa is required, especially for tight reservoirs, to constrain the pressure dependence of contact angles.

The aims of this study were to (1) improve the understanding of gas enrichment in deep basin layers through an assessment of CH<sub>4</sub>/brine/quartz contact-angle variations with increasing pressure (up to 69.4 MPa); (2) calculate the capillary resistance of deeply buried sandstone gas reservoirs; (3) devise a reliable non-destructive method for the study of wettability under high-pressure conditions; (4) quantify the influence of the contact angle on capillary resistance in a deeply buried gas reservoir; and (5) determine whether wettability at low pressures (<5 MPa) can be neglected for deeply buried reservoirs with pressures of >>5 MPa. A micro-capillary visual observation device was designed to measure high-pressure methane/brine contact angles over a pressure range of 5–69 MPa (extending the previous maximum measurement pressure of 20 MPa), representing gas reservoirs with normal pressure gradients buried at 0.5–7.0 km depths. The influence of the contact angle on gas reservoir capillary resistance and gas saturation was also considered.

## 2. Materials and Methods

**Fluids.** Methane (99.999 mol.%) and brine (2 mol·L<sup>-1</sup> CaCl<sub>2</sub> in deionized water) were used in all experiments. The methane was stored in a cylinder with an initial pressure of 12 MPa. Although higher salinity resulted in higher brine contact angles, it did not have a major influence on the angles [31,34]. For the CH<sub>4</sub>/brine/silica system, contact angles increased by <5° as salinity increased from 0 to 15 wt.% [34]. Although NaCl brine prevails in sedimentary basins, the deeply buried gas reservoirs in China are usually dominated by CaCl<sub>2</sub> brine; for example, in the Keshen gas field in the Tarim Basin [24] and the Anyue gas field in the Sichuan Basin [42]. Therefore, we used brine with a high salinity of 2 mol·L<sup>-1</sup> CaCl<sub>2</sub>. In addition, Pan et al. [31] reported that these ion types (NaCl, CaCl<sub>2</sub>, and MgCl<sub>2</sub>) only had an insignificant influence (2°) on CH<sub>4</sub> wettability (which is within experimental error). Therefore, CaCl<sub>2</sub> brine is representative of NaCl and MgCl<sub>2</sub> systems.

**High-pressure optical cell.** A capillary high-pressure optical cell (HPOC) [43,44] was developed for the methane/brine contact-angle study (Figure 1). It was constructed from a fused-quartz capillary tube measuring 665 μm for the outer diameter, 300 μm for the inner diameter, and ~20 cm in length (Polymicro Technologies, Phoenix, AZ, USA). Fluid in the HPOC could be pressurized to over 100 MPa at an ambient temperature.

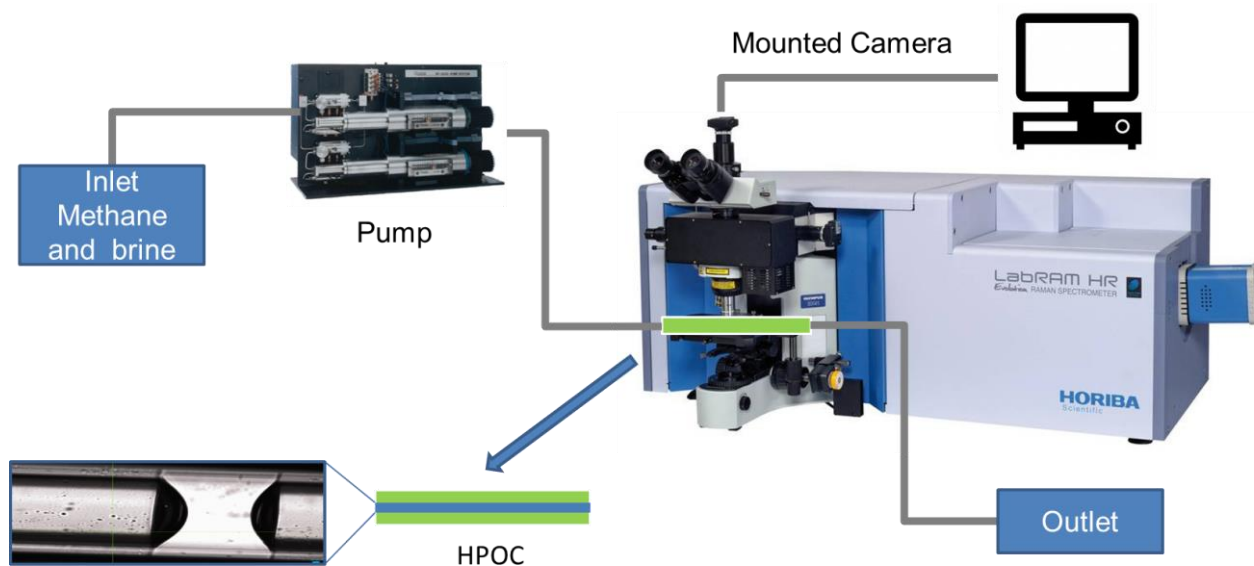


**Figure 1.** Experimental system for contact-angle observation and Raman spectra acquisition.

**Raman spectra** were obtained using a LabRAM HR Evolution (HORIBA, France) confocal Raman spectroscopy system (Figure 1). A 632.81 nm excitation beam was used with a laser focused on the HPOC through a 2.5× Olympus objective lens. The laser power was ~7.2 mW, and the spectral accuracy was ±0.2 cm. The Raman shift was measured using the Lab Spec 6 software (Horiba Scientific). The Raman test is an effective non-destructive measurement usually incorporated with a HPOC for the study of high-pressure fluids [43,45]. As the Raman shift is sensitive to fluid pressure variations, it was used to study relationships between shift and contact angle.

**Methane/brine contact-angle measurement.** There are two main existing contact-angle measuring devices. The first one is a Krüss DSA 100 instrument, using the tilted plate method [31,46]. The second one is compromised by the liquid supply part and the two-phase flow visualization part with an optical quartz capillary cell [47–49]. The contact angle data measured at reservoir conditions higher than 20 MPa are scarce. The advantage of the device used in this manuscript is that the HPOC extends the pressure range of previous optical cells by affording a high-pressure condition (higher than 45 MPa) for deeply buried reservoirs. Moreover, a Raman test was conducted while measuring the contact angle, which has rarely been achieved before. The microfluidic system included a

pump to inject methane and brine, the HPOC, and a microscope equipped with a camera and connected to a computer (Figure 1). Methane/brine interfaces within the HPOC were visualized using an Olympus (Tokyo, Japan) microscope. Photographs were captured with a high-resolution camera in the confocal Raman system through a  $2.5\times$  Olympus objective lens. Adobe Photoshop CS6 Software was used to measure the angle at the methane/brine interfaces. The burial depths of the deep reservoir were generally  $>4500$  m [50,51], so the fluid pressure was  $>45$  MPa based on the normal pressure gradient. Fluid pressures in over-pressured reservoirs are  $>45$  MPa. To ensure that the results represented most of the fluid pressures of deeply buried gas reservoirs, the maximum pressure was extended to 69 MPa. Experiments were not undertaken at higher pressures because gas leaked from the interface between the valve and the pipeline. Higher pressures will be applied in future experiments when this problem is resolved.

**Experimental procedures** are illustrated in Figure 2. Brine and methane were injected into the HPOC at a planned pressure, and the HPOC moved laterally to reach the methane/brine interface. The focal length was adjusted, and photographs were taken before acquiring the methane Raman spectra. Methane injection pressure was then increased and steps 3, 4, and 5 (Figure 2) were repeated. The experiment ended when the highest planned methane pressure was reached.

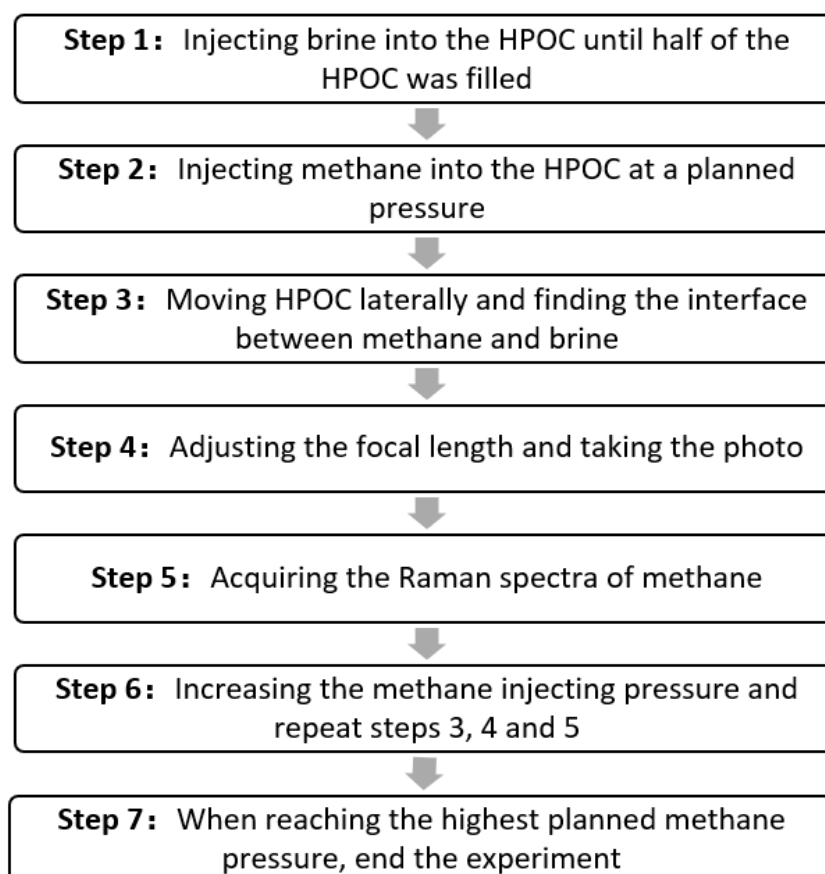


**Figure 2.** Flowchart of experimental procedure.

### 3. Experimental Results

#### 3.1. $\text{CH}_4$ /brine/Quartz Contact Angle

The phase boundary remained clear with increasing pressure in the gas columns (Figure 3A–H), with the methane/brine contact surface being curved toward the brine section (Figure 3I). The methane/brine contact interface was still clear at a pressure of 69.4 MPa, with limited property variations. The morphology of fluid in the HPOC did not change markedly at elevated pressures. The Raman technique is non-destructive, and

spectra were measured using the HPOC, so changes in the Raman shift were associated with methane pressure changes, as measured by the pressure gauge (Figure 3J). The observed decrease in the Raman shift with  $\text{CH}_4$  pressure is consistent with previous studies [47]. It was also found that phase change is not obvious in methane with increasing pressure, as the pressure–Raman shift relationship was continuous (Figure 3J). Free methane gas thus remained at the methane/brine contact interface under pressures of up to 69.4 MPa (Figure 3H). Miscible migration did not occur during hydrocarbon gas charging under high pressure (Figure 3A–H), with the capillary-force model still being followed and the capillary resistance controlling gas charging.

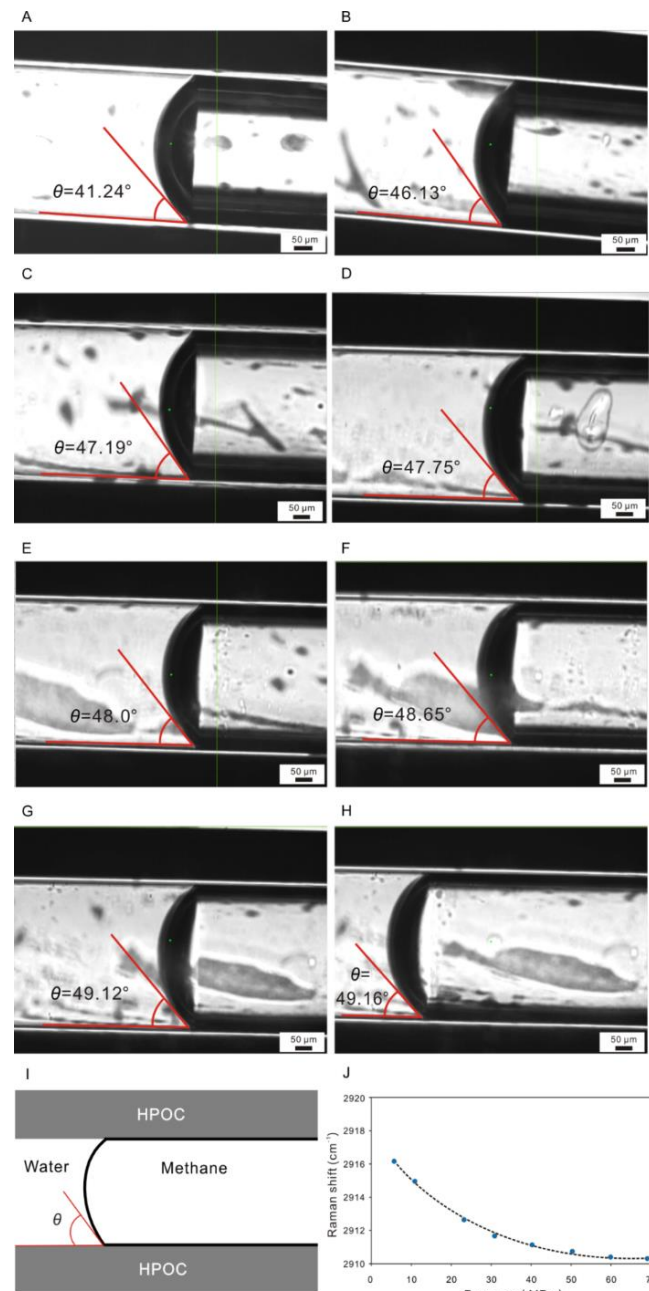


**Figure 3.** Shape of the methane/brine interface at pressures of 5.7 MPa (A); 11.5 MPa (B); 22.9 MPa (C); 30.6 MPa (D); 40.6 MPa (E); 50.1 MPa (F); 59.9 MPa (G); and 69.4 MPa (H). Schematic diagram showing the method of contact-angle measurement (I); and relationship between pressure and methane Raman shift (J).

Pressure varies with storage depth, so the methane contact angles in CH<sub>4</sub>/brine/quartz systems were measured at ultra-high pressures based on changes in the shape of the methane/brine interface (Figure 3I). Overall, the contact angle increased from 41° to 49° over a pressure range of 5.7–69.4 MPa (Table 1).

**Table 1.** CH<sub>4</sub>/brine/quartz contact angle and Raman shift for CH<sub>4</sub> at elevated pressures.

| Pressure (MPa) | $\theta$ (°) | Raman Shift (cm <sup>-1</sup> ) |
|----------------|--------------|---------------------------------|
| 5.7            | 41.24        | 2916.16                         |
| 11.5           | 46.13        | 2914.82                         |
| 22.9           | 47.19        | 2912.64                         |
| 30.6           | 47.75        | 2911.94                         |
| 40.6           | 48.00        | 2911.29                         |
| 50.1           | 48.65        | 2910.74                         |
| 59.9           | 49.12        | 2910.5                          |
| 69.4           | 49.16        | 2910.4                          |

### 3.2. Raman Shift for CH<sub>4</sub>

Raman spectra were measured for CH<sub>4</sub>. The Raman shift decreased with increasing pressure at a constant temperature. When pressure increased from 5.7 MPa, the CH<sub>4</sub> peak position of the C–H symmetric stretching band ( $\nu_1$ ) shifted to lower wavenumbers of 2916.16–2910.4 (Table 1). A linear relationship between the contact angle and the Raman shift (Figure 4) was also observed, suggesting the possibility of using the Raman shift to predict contact angles, although further study is required to confirm this.

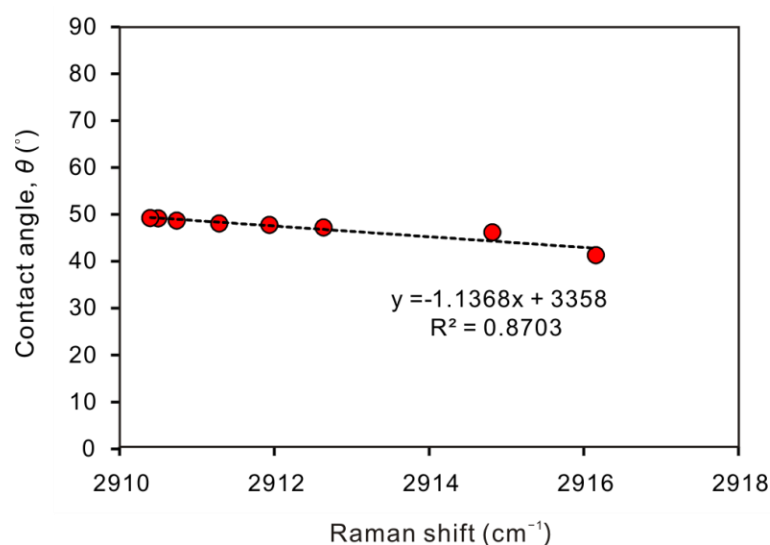


**Figure 4.** Linear relationship between contact angle and Raman shift.

## 4. Discussion

### 4.1. CH<sub>4</sub>/brine/Quartz Contact-Angle Variation with Pressure

CH<sub>4</sub>/brine/quartz contact angles were compared with those from previous studies (Figure 5). Data were previously reported at pressures of <20 MPa [34]. The contact angles measured here were higher than those of earlier studies at pressures of 0–20 MPa, possibly due to the salinity difference. The brine salinity here was 22 wt.%, compared with 1.5 wt.% in earlier studies [34]. Because the contact angle increases with salinity [34,52], higher angles were observed here, with higher solubility of brine, resulting in higher contact angles. The contact angle increased by 6° when salinity increased by 13.5 wt.%, so the salinity is estimated to be an important factor affecting the contact angle. To isolate the role of salinity, we used the brine of a deep-buried reservoir with high salinity. In addition, the

roughness of the quartz and the experimental accuracy of different methods would also influence the result; therefore, we do not expect that the results in this study will match exactly with those of Pan et al. [34]. Contact angles also increase with fluid pressure [34]. This trend is consistent with the gas/brine contact angle [53], even on different surfaces of shale [31,54], coal [55], and clay minerals [34,52]. However, at fluid pressures of >20 MPa, the influence of pressure was less obvious. With pressures increasing from 11.5 to 69.4 MPa, the contact angle increased by only 3°.

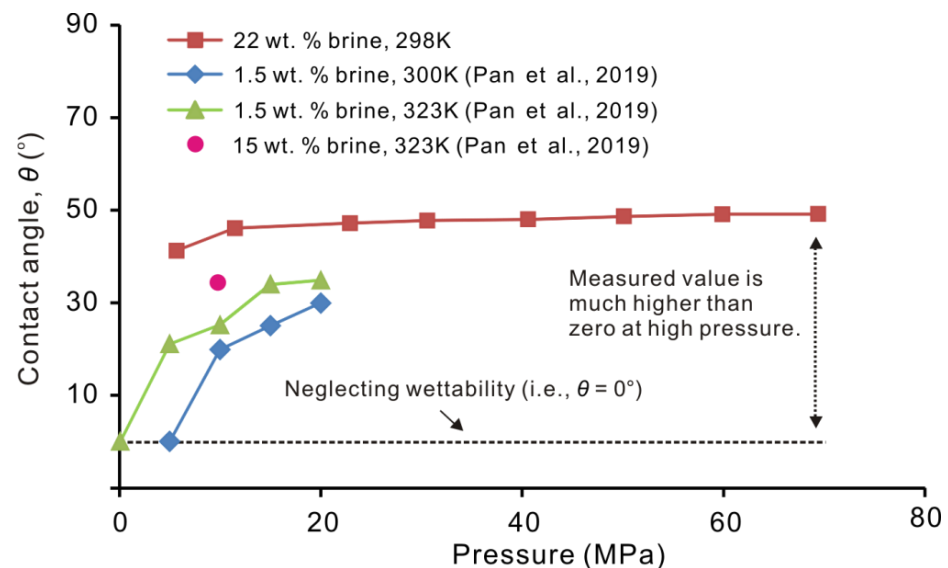


**Figure 5.** Effect of pressure on contact angle in CH<sub>4</sub>/brine/quartz systems [34].

It should also be stressed that the measured contact angle was much higher than the widely used empirical angle of 0° [41], indicating the intermediate (rather than strong) water wetness of the reservoir.

The sharp kink approximation [56,57] was applied to determine the factors affecting the contact angle [39] using the following relationship:

$$\cos \theta = \frac{\Delta \rho}{\gamma_{lg}} I - 1 \quad (2)$$

where  $\Delta \rho = \rho_{lf} - \rho_g$  ( $\rho_{lf}$  and  $\rho_g$  are densities of liquid film and gas, respectively) [54] and  $I$  is the van der Waals potential integral [58,59].

It is evident from Equation (2) that, although medium pressures influence the density difference and gas–liquid interfacial tension, the effect on density difference is much greater than that on  $\gamma_{lg}$  [60]. Because  $\rho_g$  is a direct function of pressure, any increase in pressure significantly reduces  $\Delta \rho$ , and to some extent,  $\gamma_{lg}$ . The  $\Delta \rho / \gamma_{lg}$  ratio thus decreases with pressure, increasing the contact angle on any surface [38]. In an ultra-high-pressure regime,  $\Delta \rho$ ,  $\gamma_{lg}$ , and  $\Delta \rho / \gamma_{lg}$  tend to be stable [61].

The contact angle of CH<sub>4</sub> increases with pressure due to the decreasing density difference between fluids and the stronger intermolecular interaction between CH<sub>4</sub> and the quartz/rock surface [31,40,62,63]. The methane/brine contact angle on a quartz surface is lower than that on a shale surface [31], possibly due to the difference in the van der Waals potential between CH<sub>4</sub> and the different surfaces. Organic matter in shale causes an increase in the contact angle, although in a quartz reservoir, the methane/brine contact angle is not usually affected by organic matter unless bitumen is retained before gas charging.

Physically, the influence of pressure on wettability can be attributed to the higher non-aqueous phase density [64], the consequently stronger inter-molecular interactions between CH<sub>4</sub>, the solid surface of quartz due to the increased molecular density [62,64], and the decrease in the interfacial tension between the CH<sub>4</sub> and quartz. Due to stronger

inter-molecular interactions between CH<sub>4</sub> and the quartz surface [63], and lower density differences between CH<sub>4</sub> and brine [61,62,64], the decrease in the CH<sub>4</sub>/brine/quartz contact angle occurred with increasing fluid pressure.

Studies of CH<sub>4</sub> and CO<sub>2</sub> on shale [31] and N<sub>2</sub>, Ar, SF<sub>6</sub>, and He on quartz [40] have shown that when fluid densities are similar, their wettabilities are also similar. Previous data [53] for the CO<sub>2</sub>/brine/quartz system were used to plot  $\theta$  versus CH<sub>4</sub> and CO<sub>2</sub> density (Figure 6), with density being a function of fluid temperature and pressure [65,66], as calculated using the US National Institute of Standards and Technology (NIST) Chemistry WebBook (<https://webbook.nist.gov>, accessed on 1 September 2021). When the CH<sub>4</sub> and CO<sub>2</sub> densities were approaching a supercritical state, their brine contact angles became similar: CH<sub>4</sub> and CO<sub>2</sub> densities of 249.5 and 252.6 kg m<sup>-3</sup> were related to  $\theta$  values of 48° and 47.8°, respectively. The contact angles matched well when CH<sub>4</sub> and CO<sub>2</sub> had similar densities, indicating that gas density strongly influences the contact angle on the same surface, even with different gases. Previous studies [31] have shown that with CO<sub>2</sub>/brine/quartz at high densities, CO<sub>2</sub> reaches a high density under a much lower pressure than CH<sub>4</sub>. This provides the possibility of predicting CH<sub>4</sub>/brine/quartz contact angles under high pressures by combining CH<sub>4</sub> and CO<sub>2</sub> data with Equation (3), gradually increasing in the range of 50°–60° under higher pressures on a quartz surface.

$$\theta = 29.45 \rho_g^{0.0922} \quad (3)$$

where  $\theta$  relates to CH<sub>4</sub>/brine/quartz, and  $\rho_g$  represents the density of CH<sub>4</sub>.

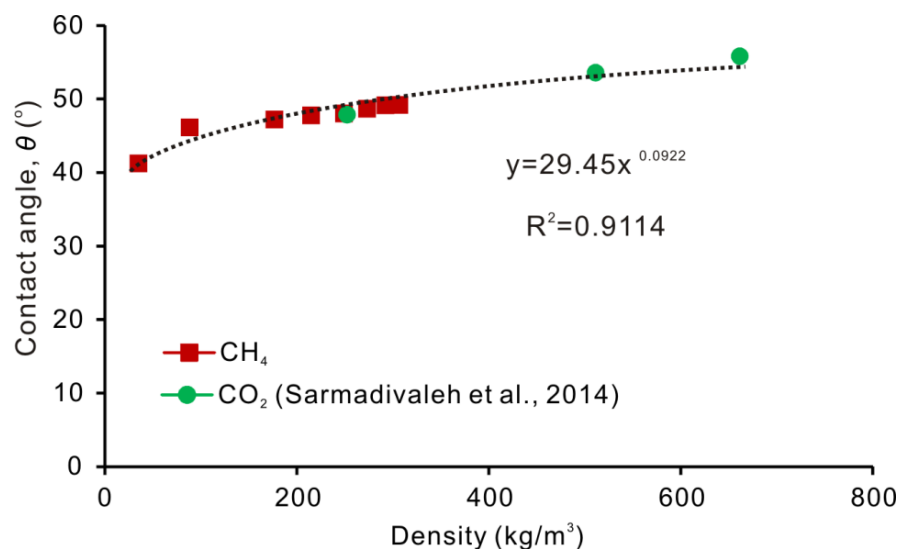


**Figure 6.** Effect of fluid density on contact angle in the CH<sub>4</sub>/brine/quartz and CO<sub>2</sub>/brine/quartz systems [53].

#### 4.2. Raman Shift Variation with Contact Angle

Increasing CH<sub>4</sub> density causes a decrease in the Raman shift [67,68]. At the same time, the contact angle increases with increasing pressure. As a result, a negative relationship between the Raman shift and the contact angle was observed. Mechanically, according to hard sphere models of fluids [69], increasing pressure results in the increasing density of a molecular fluid [61]. The peak position initially shifts to a lower wavenumber (lower energy), followed by a minimum, and then shifts to a higher wavenumber (higher energy) while pressure increases at a constant temperature [68]. In other words, the inter-molecular forces are dominated by van der Waals-type attractive forces until a certain density (i.e., 300 kg m<sup>-3</sup>) is reached, at which repulsive forces between hard spheres begin to dominate the inter-molecular potential [68]. Moreover, there exist stronger inter-molecular interactions between CH<sub>4</sub> and the quartz surface [63], combined with lower density differences between CH<sub>4</sub> and brine [61], and the decrease in the CH<sub>4</sub>/brine/quartz

contact angle occurred with increasing fluid pressure [62,64]; therefore, the Raman peak position of CH<sub>4</sub> shifted to a lower wavenumber when there was an increased contact angle.

### 4.3. Capillary Resistance of Deeply Buried Gas Reservoirs

Taking a hypothetical sandstone gas reservoir as an example (Table 2), we see that it becomes more severely compacted with increasing burial depth, with the pore-throat radius decreasing exponentially with increasing depth [45,70]. As burial depth increases from 1000 m to 4000 m, pore radii decrease from 1.1 μm to 0.1 μm. However, over a depth range of 4000–7000 m, the pore radius becomes stable at ~0.1 μm (Figure 7A), assuming a formation pressure gradient of 10 MPa km<sup>-1</sup>, temperature gradient of 30 °C km<sup>-1</sup>, and surface temperature of 15 °C. Based on Equation (1), capillary resistance at different depths may be calculated from the contact angle, interfacial tension [61], and pore-throat radius at different depths (Figure 7B–D). At the appropriate wettability, the contact angle was obtained by calculating gas density at each depth using Equation (3) (Table 2). Capillary resistance calculated from the measured contact angle is generally much lower than that based on the empirical parameter ( $\theta = 0^\circ$ ) [41], indicating that the previously applied simplification of the empirical methane/brine contact angle results in a substantial overestimation of the capillary resistance of gas reservoirs.

**Table 2.** Comparison between capillary resistances when incorporating or neglecting wettability.

| Depth (m) | Temperature (K) | Pressure (MPa) | r (10 <sup>-6</sup> m) | $\rho_g$ (kg m <sup>-3</sup> ) | $\rho_w$ (kg m <sup>-3</sup> ) | IFT, $\gamma_{lg}$ (mN m <sup>-1</sup> ) | $\theta$ (°) | Capillary Resistance (MPa)   |  |
|-----------|-----------------|----------------|------------------------|--------------------------------|--------------------------------|--|--------------|------------------------------|--|
|           |                 |                |                        |                                |                                |  |              | Incorporation of Wettability | Neglecting Wettability (i.e., $\theta = 0^\circ$ ) |
| 1000      | 318             | 10             | 0.13                   | 68                             | 1065                           | 58.56                                    | 43.47        | 0.65                         | 0.90   |
| 2000      | 348             | 20             | 0.026                  | 120                            | 1052                           | 51.67                                    | 45.81        | 2.77                         | 3.97   |
| 3000      | 378             | 30             | 0.013                  | 151                            | 1037                           | 45.64                                    | 46.80        | 4.81                         | 7.02   |
| 4000      | 408             | 40             | 0.0097                 | 171                            | 1019                           | 40.21                                    | 47.33        | 5.62                         | 8.29   |
| 5000      | 438             | 50             | 0.0092                 | 185                            | 997                            | 35.47                                    | 47.66        | 5.19                         | 7.71   |
| 6000      | 468             | 60             | 0.009                  | 194                            | 975                            | 30.03                                    | 47.88        | 4.48                         | 6.67   |
| 7000      | 498             | 70             | 0.009                  | 202                            | 952                            | 27.6                                     | 48.05        | 4.10                         | 6.13   |

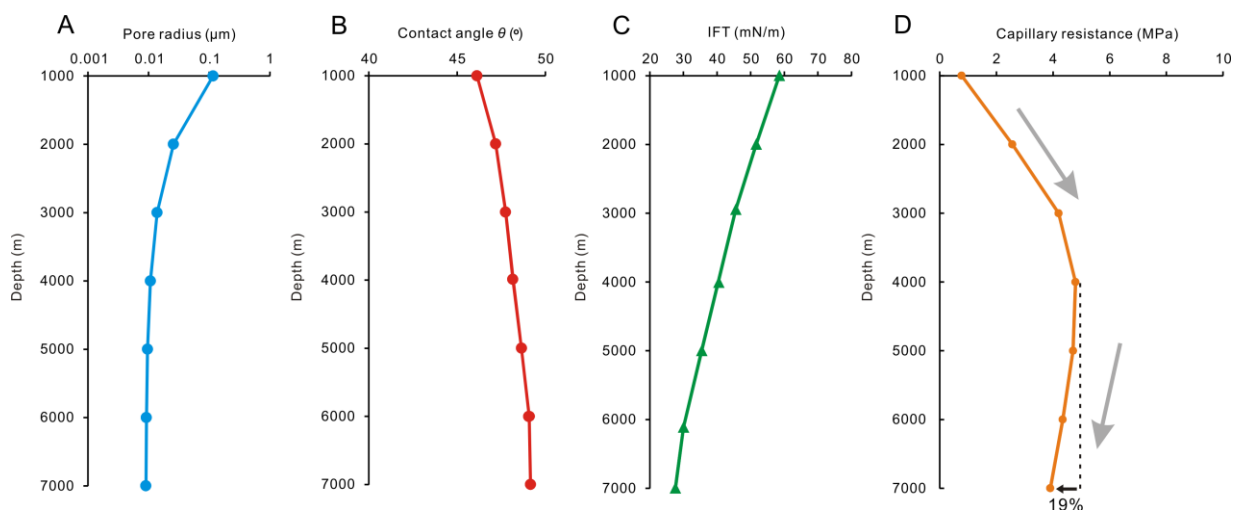


**Figure 7.** Gas reservoir pore radius (A); contact angle (B); interfacial tension (IFT) (C); and capillary resistance (D) at burial depths of 1000–7000 m.

Capillary resistance changed when considering or neglecting wettability (i.e.,  $\theta = 0^\circ$ ) (Table 2). When neglecting wettability, a contact angle of  $0^\circ$  was used at each burial depth. The difference between the two conditions indicates the influence of wettability on gas storage. Capillary resistance calculated from the measured contact angle was generally 33% lower than that based on the empirical value ( $\theta = 0^\circ$ ), indicating that the previously applied

simplification that neglects wettability results in a substantial overestimation of the capillary resistance of gas reservoirs. When considering reservoir wettability, the capillary resistance for gas entering the reservoir decreases and the relative gas permeability increases, which promotes charging and seepage of natural gas [71,72].

The variation of capillary resistance as a function of depth indicates that with increasing burial depth, the natural gas charging resistance first increases then decreases (Figure 7D). As depth increases from 1000 to 4000 m, capillary resistance increases from 0.8 to 4.8 MPa, mainly owing to the sharp decrease in the capillary radius. At depths of 4500–7000 m, the capillary radius tends to be stable and capillary resistance decreases due to the decreasing contact angle and interfacial tension, with natural gas charging and migration resistance decreasing by 19% over a range of 3.9–4.8 MPa.

Without considering the change of wettability and interfacial tension, the capillary resistance is controlled by the pore throat. The pore throat of the reservoir decreases with increasing burial depth, resulting in increased capillary resistance [73]. However, without considering the change in pore diameter, the contact angle and interfacial tension decrease with increasing depth, with decreasing capillary resistance. Therefore, in both scenarios, both an increase and decrease with burial depth are possible. Owing to the predominant effect of pore diameter, capillary resistance initially decreases with depth and passes through a maximum before decreasing again due to the influence of the decreasing contact angle and interfacial tension at greater depth. The maximum capillary resistance occurs at ~4000 m depth. There are few reports of the point of inflection in capillary resistance.

Therefore, under a certain reservoir charging pressure, the reservoir capillary resistance is reduced, which is conducive to gas charging into smaller pore throats with the discharge of brine. The gas then occupies more reservoir space with higher gas saturation. The presumed low gas saturation of deep reservoirs should therefore be re-evaluated, as many natural gas resources may be buried at a substantial depth.

## 5. Conclusions

Deeply buried tight sandstone reservoirs are important fuel resources, and CH<sub>4</sub> wettability is important for determining capillary resistance and gas saturation. However, CH<sub>4</sub> wettability at high pressures (>20 MPa) is poorly understood. The traditionally accepted empirical CH<sub>4</sub> contact angle of 0° is misleading because it implies that tight reservoirs have low gas saturation levels due to high capillary resistance. We used a micro-capillary visual observation device to measure contact angles in the CH<sub>4</sub>/brine/quartz system at pressures of up to 69.4 MPa and developed a method of predicting the contact angle based on gas density. We also examined their influence on gas charge resistance and gas saturation. The results led to the following conclusions:

- (a) With a pressure increase from 5.7 to 11.5 MPa, the methane/brine contact angle increases from 41° to 46°, consistent with published data. However, when pressures increase from 11.5 to 69.4 MPa, the contact angle increases by only 3°, as the interfacial tension and density difference between gas and brine is stable.
- (b) Capillary resistance calculated from the measured contact angle is much lower than that based on the empirical parameter ( $\theta = 0^\circ$ ). The previously applied simplification of the empirical methane/brine contact angle results in a large overestimation (33%) of gas reservoir capillary resistance.
- (c) As the burial depth increases from 4500 to 7000 m, the natural gas charging resistance decreases from 4.8 to 3.9 MPa, reducing by 19%, owing to the decreases in the contact angle and interfacial tension. The presumed low gas saturation of deep reservoirs should therefore be re-evaluated.
- (d) The Raman shift decreases with an increasing contact angle. This non-destructive method could be used to predict contact angles by measuring the Raman shift of the HOPC and fluid inclusions in the reservoir. In future studies, the measurement system may be applied in the exploration of high-pressure oil/brine and gas/oil contact angles.

**Author Contributions:** Conceptualization, H.T.; Methodology, J.F., Q.L. and X.L.; Resources, J.F.; Writing of original draft, H.T.; Editing, Z.Y. All authors have read and agreed to the published version of the manuscript.

**Funding:** This work was supported by the National Natural Science Foundation of China (Grants 42002177 and 41902045) and the PetroChina R&D Program (Grants 2021DJ0104 and YGJ2019–05).

**Data Availability Statement:** Data are available from the corresponding authors upon request.

**Acknowledgments:** Authors thank Gaus Garri from RWTH Aachen University for their assistance and advice on contact-angle analysis.

**Conflicts of Interest:** The authors declare no conflict of interest.

## Abbreviations

|                 |                            |
|-----------------|----------------------------|
| HPOC            | High-pressure optical cell |
| CH <sub>4</sub> | Methane                    |
| CO <sub>2</sub> | Carbon dioxide             |
| N <sub>2</sub>  | Nitrogen                   |
| Ar              | Argon                      |
| SF <sub>6</sub> | Sulfur hexafluoride        |
| He              | Helium                     |
| IFT             | Interfacial tension        |

## References

- Hubbert, M.K.; Rubey, W.W. Role of fluid pressure in mechanics of overthrust faulting: I. mechanics of fluid-filled porous solids and its application to overthrust faulting. *Geol. Soc. Am. Bull.* **1959**, *5*, 115–166. [\[CrossRef\]](#)
- Ingram, G.M.; Urai, J.; Naylor, M.A. Sealing processes and top seal assessment. *Nor. Pet. Soc. Spec. Publ.* **1997**, *97*, 165–174. [\[CrossRef\]](#)
- Hildenbrand, A.; Schlömer, S.; Krooss, B.M. Gas breakthrough experiments on fine-grained sedimentary rocks. *Geofluids* **2010**, *1*, 3–23. [\[CrossRef\]](#)
- Lenormand, R.; Zarcone, C.; Sarr, A. Mechanisms of the displacement of one fluid by another in a network of capillary ducts. *J. Fluid Mech.* **1983**, *135*, 337–353. [\[CrossRef\]](#)
- McCreesh, C.A.; Ehrlich, R.; Crabtree, S.J.; McCreesh, C.A.; Ehrlich, R.; Crabtree, S.J. Petrography and reservoir physics II: Relating thin section porosity to capillary pressure, the association between pore types and throat size. *AAPG Bull. De Biol. Clin.* **1991**, *10*, 1563–1578. [\[CrossRef\]](#)
- Blunt, M.J.; Bijeljic, B.; Dong, H.; Gharbi, O.; Iglauer, S.; Mostaghimi, P.; Paluszny, A.; Pentland, C. Pore-scale imaging and modelling. *Adv. Water Resour.* **2013**, *51*, 197–216. [\[CrossRef\]](#)
- Sang, I.H.; Lee, K.P.; Dong, S.L.; Powers, S.E. Effects of fractional wettability on capillary pressure-saturation-relative permeability relations of two-fluid systems. *Adv. Water Resour.* **2006**, *2*, 212–226. [\[CrossRef\]](#)
- Rabbani, H.S.; Joekar-Niasar, V.; Shokri, N. Effects of intermediate wettability on entry capillary pressure in angular pores. *J. Colloid Interface Sci.* **2016**, *473*, 34–43. [\[CrossRef\]](#)
- Iglauer, S.; Pentland, C.H.; Busch, A. CO<sub>2</sub> wettability of seal and reservoir rocks and the implications for carbon geo-sequestration. *Water Resour. Res.* **2015**, *1*, 729–774. [\[CrossRef\]](#)
- Iglauer, S.; Al-Yaseri, A.Z.; Wolff-Boenisch, D. Basalt-CO<sub>2</sub>-brine wettability at storage conditions in basaltic formations. *Int. J. Greenh. Gas Control* **2020**, *102*, 103148. [\[CrossRef\]](#)
- Olugbenga, F.; Edo, M. Wettability effects on capillary pressure, relative permeability, and irreducible saturation using porous plate. *J. Pet. Eng.* **2014**, *2014*, 465418. [\[CrossRef\]](#)
- Gravelle, S.; Ybert, C.; Bocquet, L.; Joly, L. Anomalous capillary filling and wettability reversal in nanochannels. *Phys. Rev. E* **2016**, *93*, 033123. [\[CrossRef\]](#) [\[PubMed\]](#)
- Grate, J.W.; Dehoff, K.J.; Warner, M.G.; Pittman, J.W.; Wietsma, T.W.; Zhang, C.; Oostrom, M. Correlation of oil-water and air-water contact angles of diverse silanized surfaces and relationship to fluid interfacial tensions. *Langmuir* **2012**, *28*, 7182–7188. [\[CrossRef\]](#)
- Feng, Z.; Tang, H.; Meng, Y.; Gao, L.; Xing, X. Damage evaluation for water-based underbalanced drilling in low-permeability and tight sandstone gas reservoirs. *Pet. Explor. Dev.* **2009**, *36*, 113–119. [\[CrossRef\]](#)
- Quang, T.; Leong, F.Y.; An, H.; Tan, B.H.; Ohl, C.D. Growth and wetting of water droplet condensed between micron-sized particles and substrate. *Sci. Rep.* **2016**, *6*, 30989. [\[CrossRef\]](#)
- Anderson; William, G. Wettability literature survey, Part1: Rock/oil/brine interactions and the effects of core handling on wettability. *J. Pet. Technol.* **1986**, *38*, 1125–1144. [\[CrossRef\]](#)

17. Chiquet, P.; Broseta, D.; Thibeau, S. Wettability alteration of caprock minerals by carbon dioxide. *Geofluids* **2007**, *7*, 112–122. [[CrossRef](#)]
18. Valvatne, P.H.; Blunt, M.J. Predictive pore-scale modeling of two-phase flow in mixed wet media. *Water Resour. Res.* **2004**, *40*, 187. [[CrossRef](#)]
19. Auset, M.; Keller, A.A. Pore-scale visualization of colloid straining and filtration in saturated porous media using micromodels. *Water Resour. Res.* **2006**, *42*, W12S02. [[CrossRef](#)]
20. Yang, Y.; Yao, J.; Dijke, M. Effect of reservoir rock wettability on microcosmic distribution of residual oil after gas displacement. *Acta Pet. Sin.* **2010**, *31*, 467–470. [[CrossRef](#)]
21. Burke, L.; Nevison, G. Improved Hydraulic Fracture Performance with Energized Fluids: A Montney Example. In Proceedings of the SPE Eastern Regional Meeting, Columbus, Ohio, USA, 17–19 August 2011. [[CrossRef](#)]
22. Borysenko, A.; Clennell, B.; Sedev, R.; Burgar, I.; Ralston, J.; Raven, M.; Dewhurst, D.; Liu, K. Experimental investigations of the wettability of clays and shales. *J. Geophys. Res.* **2009**, *114*, B07202. [[CrossRef](#)]
23. Pang, X.Q.; Jia, C.Z.; Wang, W.Y. Petroleum geology features and research developments of hydrocarbon accumulation in deep petroliferous basins. *Pet. Sci.* **2015**, *12*, 1–53. [[CrossRef](#)]
24. Lu, X.; Yu, Z.; Liu, K.; Zhao, M.; Fan, J.; Guo, X.; Zhuo, Q.; Gui, L. Transformation of a large ancient oil reservoir to a dry gas reservoir: A case study of the Kela-2 gas field in the Kuqa foreland basin, NW China. *Geofluids* **2022**, *2022*, 6615336. [[CrossRef](#)]
25. Cxa, B.; Mw, A.; Sh, A. Petroleum emplacement inhibits quartz cementation and feldspar dissolution in a deeply buried sandstone. *Mar. Pet. Geol.* **2020**, *118*, 104449. [[CrossRef](#)]
26. Hunter, T.N.; Jameson, G.J.; Wanless, E.J.; Dupin, D.; Armes, S.P. Adsorption of submicrometer-sized cationic sterically stabilized polystyrene latex at the air-water interface: Contact angle determination by ellipsometry. *Langmuir* **2009**, *25*, 3440–3449. [[CrossRef](#)]
27. Mirchi, V.; Saraji, S.; Goual, L.; Piri, M. Dynamic interfacial tensions and contact angles of surfactant-in-brine/oil/shale systems: Implications to enhanced oil recovery in shale oil reservoirs. In Proceedings of the SPE Improved Oil Recovery Symposium, Tulsa, OK, USA, 12–16 April 2014. [[CrossRef](#)]
28. Nishino, T.; Meguro, M.; Nakamae, K.; Matsushita, M.; Ueda, Y. The lowest surface free energy based on -CF<sub>3</sub> alignment. *Langmuir* **1999**, *15*, 4321–4323. [[CrossRef](#)]
29. Arkles, B.; Pan, Y.; Kim, Y.M. *The Role of Polarity in the Structure of Silanes Employed in Surface Modification*; Mittal, K.L., Ed.; Silanes and Other Coupling Agents Volume 5; CRC Press: Boston, MA, USA, 2009; pp. 51–64.
30. Wong, T.S.; Ho, C.M. Dependence of macroscopic wetting on nanoscopic surface textures. *Langmuir* **2009**, *25*, 12851–12854. [[CrossRef](#)]
31. Pan, B.; Li, Y.; Wang, H.; Jones, F.; Iglauer, S. CO<sub>2</sub> and CH<sub>4</sub> wettabilities of organic-rich shale. *Energy Fuels* **2018**, *32*, 1914–1922. [[CrossRef](#)]
32. Abdi, J.; Amar, M.N.; Hadipoor, M.; Gentzis, T.; Hemmati-Sarapardeh, A.; Ostadhassan, M. Modeling of Brine/CO<sub>2</sub>/Mineral Wettability Using Gene Expression Programming (GEP): Application to Carbon Geo-Sequestration. *Minerals* **2022**, *12*, 760. [[CrossRef](#)]
33. Jiang, H.; Gao, Y.; Khoso, S.A.; Ji, W.; Hu, Y. Interpretation of Hydrophobization Behavior of Dodecylamine on Muscovite and Talc Surface through Dynamic Wettability and AFM Analysis. *Minerals* **2018**, *8*, 391. [[CrossRef](#)]
34. Pan, B.; Jones, F.; Huang, Z.; Yang, Y.; Li, Y.; Hejazi, S.H.; Iglauer, S. Methane (CH<sub>4</sub>) wettability of clay-coated quartz at reservoir conditions. *Energy Fuels* **2019**, *33*, 788–795. [[CrossRef](#)]
35. Roshan, H.; Al-Yaseri, A.Z.; Sarmadivaleh, M.; Iglauer, S. On wettability of shale rocks. *J. Colloid Interface Sci.* **2016**, *475*, 104–111. [[CrossRef](#)] [[PubMed](#)]
36. De Ruijter, M.; Kölsch, P.; Voué, M.; De Coninck, J.; Rabe, J.P. Effect of temperature on the dynamic contact angle. *Colloids Surf. A Physicochem. Eng. Asp.* **1998**, *144*, 235–243. [[CrossRef](#)]
37. Saraji, S.; Piri, M.; Goual, L. The effects of SO<sub>2</sub> contamination, brine salinity, pressure, and temperature on dynamic contact angles and interfacial tension of supercritical CO<sub>2</sub>/brine/quartz systems. *Int. J. Greenh. Gas Control.* **2014**, *28*, 147–155. [[CrossRef](#)]
38. Arif, M.; Barifcani, A.; Iglauer, S. Solid/CO<sub>2</sub> and solid/water interfacial tensions as a function of pressure, temperature, salinity and mineral type: Implications for CO<sub>2</sub> wettability and CO<sub>2</sub> geo-storage. *Int. J. Greenh. Gas Control* **2016**, *53*, 263–273. [[CrossRef](#)]
39. Al-Yaseri, A.Z.; Roshan, H.; Zhang, Y.; Rahman, T.; Lebedev, M.; Barifcani, A.; Iglauer, S. Effect of the temperature on CO<sub>2</sub>/brine/dolomite wettability: Hydrophilic versus hydrophobic surfaces. *Energy Fuels* **2017**, *31*, 6329–6333. [[CrossRef](#)]
40. Al-Yaseri, A.Z.; Roshan, H.; Lebedev, M.; Barifcani, A.; Iglauer, S. Dependence of quartz wettability on fluid density. *Geophys. Res. Lett.* **2016**, *43*, 3771–3776. [[CrossRef](#)]
41. Ahmed, T. Fundamentals of Rock Properties. Ahmed, T.; *Reservoir Engineering Handbook*, 5th ed.; Elsevier: Oxford, UK, 2019; Chapter 4; pp. 167–281.
42. Li, Y.; Qin, S.; Wang, Y.; Holland, G.; Zhou, Z. Tracing interaction between hydrocarbon and groundwater systems with isotope signatures preserved in the Anyue gas field, central Sichuan Basin, China. *Geochim. Et Cosmochim. Acta* **2020**, *274*, 261–285. [[CrossRef](#)]
43. Chou, I.M.; Bassett, W.A.; Anderson, A.J.; Mayanovic, R.A.; Shang, L. Containment of fluid samples in the hydrothermal diamond-anvil cell without the use of metal gaskets: Performance and advantages for in situ analysis. *Rev. Sci. Instrum.* **2008**, *79*, 393. [[CrossRef](#)]

44. Wang, J.; Zhou, S.; Bei, K.; Zhang, D.; Chou, I.M.; Chen, Z.; Lin, C.; Pan, Z. Using fused silica capillary cell and in situ Raman spectroscopy to develop a set-up for measurement the volume expansion of carbon dioxide + n-hexane. *Energy Fuels* **2017**, *31*, 6314–6319. [[CrossRef](#)]
45. Guo, H.; Chen, Y.; Lu, W.; Li, L.; Wang, M. In situ raman spectroscopic study of diffusion coefficients of methane in liquid water under high pressure and wide temperatures. *Fluid Phase Equilibria* **2013**, *360*, 274–278. [[CrossRef](#)]
46. Lander, L.M.; Siewierski, L.M.; Brittain, W.J.; Vogler, E.A. A systematic comparison of contact angle methods. *Langmuir* **1993**, *9*, 2237–2239. [[CrossRef](#)]
47. Barajas, A.M.; Panton, R.L. The effects of contact angle on two-phase flow in capillary tubes. *Int. J. Multiph. Flow* **1993**, *2*, 337–346. [[CrossRef](#)]
48. Qu, J.; Wang, Q.; Li, C.; Han, X.; He, Z. A simple model for Taylor flow induced contact angle hysteresis and capillary pressure inside mini/micro-scale capillary tubes. *Int. J. Heat Mass Transf.* **2014**, *78*, 1004–1007. [[CrossRef](#)]
49. Wang, C.; Tian, M.; Zhang, J.; Zhang, G. Experimental study on liquid-liquid two-phase flow patterns and plug hydrodynamics in a small channel. *Exp. Therm. Fluid Sci.* **2021**, *129*, 110455. [[CrossRef](#)]
50. Tian, H.; Zou, C.; Liu, S.; Zhang, S.; Yuan, M. Gas physical properties and their implication on gas saturation and leakage in deep reservoirs: A case study of Cambrian gas field, Sichuan Basin, China. In Proceedings of the International Petroleum Technology Conference, Beijing, China, 26–28 March 2019. [[CrossRef](#)]
51. Zhao, W.; Zhang, S.; He, K.; Zeng, H.; Hu, G.; Zhang, B.; Wang, Z.; Li, Y. Origin of conventional and shale gas in Sinian–lower Paleozoic strata in the Sichuan Basin: Relayed gas generation from liquid hydrocarbon cracking. *AAPG Bulletin*. **2019**, *103*, 1265–1296. [[CrossRef](#)]
52. Siddiqui, M.A.Q.; Ali, S.; Fei, H.; Roshan, H. Current understanding of shale wettability: A review on contact angle measurements. *Earth-Sci. Rev.* **2018**, *181*, 1–11. [[CrossRef](#)]
53. Sarmadivaleh, M.; Al-Yaseri, A.Z.; Iglauer, S. Influence of temperature and pressure on quartz-water-CO<sub>2</sub> contact angle and CO<sub>2</sub>-water interfacial tension. *J. Colloid Interface Sci.* **2015**, *441C*, 59–64. [[CrossRef](#)]
54. Kaveh, N.S.; Barnhoorn, A.; Wolf, K.K. Wettability evaluation of silty shale caprocks for CO<sub>2</sub> storage. *Int. J. Greenh. Gas Control* **2016**, *49*, 425–435. [[CrossRef](#)]
55. Saghafi, A.; Javanmard, H.; Pinetown, K. Study of coal gas wettability for CO<sub>2</sub> storage and CH<sub>4</sub> recovery. *Geofluids* **2014**, *14*, 310–325. [[CrossRef](#)]
56. Dietrich, S.; Napiórkowski, M. Analytic results for wetting transitions in the presence of van der Waals tails. *Phys. Rev. A* **1991**, *43*, 1861–1885. [[CrossRef](#)] [[PubMed](#)]
57. Merath, C. Microscopic Calculation of Line Tensions. Ph.D. Thesis, Institute for Theoretical and Applied Physics, University of Stuttgart, Stuttgart, Germany, 2008.
58. Gatica, S.M.; Johnson, J.K.; Zhao, X.C.; Cole, M.W. Wetting transition of water on graphite and other surfaces. *J. Phys. Chem. B* **2004**, *108*, 11704–11708. [[CrossRef](#)]
59. Garcia, R.; Osborne, K.; Subashi, E. Validity of the “sharp-kink approximation” for water and other fluids. *J. Phys. Chem. B* **2008**, *112*, 8114–8119. [[CrossRef](#)]
60. Georgiadis, A.; Maitland, G.; Trusler, J.; Bismarck, A. Interfacial tension measurements of the (H<sub>2</sub>O+CO<sub>2</sub>) system at elevated pressures and temperatures. *Euroeconomica* **2010**, *94*, 7–14. [[CrossRef](#)]
61. Kashefi, K.; Pereira, L.; Chapoy, A.; Burgass, R.; Tohidi, B. Measurement and modelling of interfacial tension in methane/water and methane/brine systems at reservoir conditions. *Fluid Phase Equilibria* **2016**, *409*, 301–311. [[CrossRef](#)]
62. Rahman, T.; Lebedev, M.; Barifcani, A.; Iglauer, S. Residual trapping of supercritical CO<sub>2</sub> in oil-wet sandstone. *J. Colloid Interface Sci.* **2016**, *469*, 63–68. [[CrossRef](#)] [[PubMed](#)]
63. Iglauer, S. CO<sub>2</sub>-water-rock wettability: Variability, influencing factors, and implications for CO<sub>2</sub> geostorage. *Acc. Chem. Res.* **2017**, *50*, 1134. [[CrossRef](#)] [[PubMed](#)]
64. Al-Yaseri, A.Z.; Lebedev, M.; Barifcani, A.; Iglauer, S. Receding and advancing (CO<sub>2</sub>+ brine+ quartz) contact angles as a function of pressure, temperature, surface roughness, salt type and salinity. *J. Chem. Thermodyn.* **2016**, *93*, 416–423. [[CrossRef](#)]
65. Setzmann, U.; Wagner, W. A new equation of state and tables of thermodynamic properties for methane covering the range from the melting line to 625K at pressures up to 100 MPa. *J. Phys. Chem. Ref. Data* **1991**, *20*, 1061–1155. [[CrossRef](#)]
66. Span, R.; Wagner, W. A new equation of state for carbon dioxide covering the fluid region from the triple-point temperature to 1100K at pressures up to 800 MPa. *J. Phys. Chem. Ref. Data* **1996**, *25*, 1509–1596. [[CrossRef](#)]
67. Fabre, D.; Couty, R. Investigation on the density effects in the Raman spectrum of methane up to 3.000 bar. Application to the determination of pressure in fluid inclusions trapped in minerals. *Comptes Rendus De L'académie Des Sci. Série II. Mech. Phys. Chem. Space Sciences. Earth Sci.* **1986**, *303*, 1305–1308.
68. Lu, W.; Chou, I.M.; Burruss, R.C.; Song, Y. A unified equation for calculating methane vapor pressures in the CH<sub>4</sub>-H<sub>2</sub>O system with measured Raman shifts. *Geochim. Et Cosmochim. Acta* **2007**, *71*, 3969–3978. [[CrossRef](#)]
69. Ben-Amotz, D.; Herschbach, D.R. Hard fluid model for solvent-induced shifts in molecular vibrational frequencies. *J. Phys. Chem.* **1993**, *97*, 2295–2306. [[CrossRef](#)]
70. Fox, D.M.; Bryan, R.B.; Fox, C.A. Changes in pore characteristics with depth for structural crusts. *Geoderma* **2004**, *120*, 109–120. [[CrossRef](#)]

71. Lu, X.; Zhao, M.; Liu, K.; Zhuo, Q.; Fan, J.; Yu, Z.; Gong, Y. Formation condition of deep gas reservoirs in tight sandstones in kuqa foreland basin. *Pet. Res.* **2018**, *004*, 346–358. [[CrossRef](#)]
72. Tian, H.; Wang, M.; Liu, S.; Zhang, S.; Zou, C. Influence of Pore Water on the Gas Storage of Organic-Rich Shale. *Energy Fuels* **2020**, *34*, 5293–5306. [[CrossRef](#)]
73. Jiang, H.; Pang, X.; Chen, D.; Chen, D. Effective sandstone reservoir determination and quantitative evaluation of deep strata in Kuqa depression, Tarim Basin. *Acta Pet. Sin.* **2015**, *36*, 112–119. [[CrossRef](#)]

**Disclaimer/Publisher’s Note:** The statements, opinions and data contained in all publications are solely those of the individual author(s) and contributor(s) and not of MDPI and/or the editor(s). MDPI and/or the editor(s) disclaim responsibility for any injury to people or property resulting from any ideas, methods, instructions or products referred to in the content.